The Hebrew University of Jerusalem
Faculty of Science
The School of Computer Science and Engineering

Using the AC Stark Effect to Modify the Refractive Index of Rubidium Vapor

Raphael David Cohen
326832664
Supervisor: Dr. Nadav Katz
Thesis submitted for the degree of Master of Science

May 6, 2013

Abstract

Experimental and theoretical work is done to develop a method of refractive index engineering with lasers in a heated Rubidium vapor. It is shown that a strong control laser far detuned from an atomic resonance (> 1 GHz) can be used to modify the refractive index. This resulting change in refractive index may be used to create photonic structures. With this technique a thick Bragg grating is created. Experimental results are presented and shown to agree well with theory and simulation.

Contents

List of Figures

Acknowledgments

I would like to thank Dr. Nadav Katz for his ideas, support, patience and encouragement. David Shwa, for his advice, experience, ideas, support and everything that he has taught me about optics and experimental techniques, without his invaluable assistance this work would not have succeeded. Prof. John Howell, for his ideas which were the springboard for this work. All the members of The Macroscopic Quantum Coherence Group, Dr Felix Zeides, Dr. Yoni Shalibo, Roi Resh, Elisha Svetitsky, Ofer Fogel for their help and assistance and everything I have learnt from them. Dr. Stephen Wiesner for useful discussions and ideas. I would also like to thank all my teachers on the Masters course in Applied Physics here at the Hebrew University - so much of what they taught me has proved invaluable in this thesis from atomic susceptibility, quantum mechanics, optics, lasers, Jones matrices, electro-optic effect, Bragg gratings and more. Finally I would like to thank my family especially the patience and encouragement of my wife. I hope one day my kids will find the experiments in the lab more interesting than the fish outside.

1 Introduction

The ability to control light is of great importance in modern technology and hence society [1, 2]. One of the main ways of controlling light is through the transmission properties of the media. This includes both the phase and absorption of the radiation, through the complex refractive index of the media. Constructing materials with well defined and controlled refractive index properties has led to the development of a whole world of devices (such as lenses, waveguides, couplers, gratings) that are integral to current technologies.

The main methods of refractive control employ a solid infrastructure where the refractive index contrast is designed into the material. The remarkable control in manufacturing these materials has enabled the development of a myriad of devices, providing the infrastructure for large parts of modern technology, especially in communications. Given the breadth of applications of optics and photonics, it is not surprising that there is interest in finding different ways of using light matter interactions to control light. Over the years a variety of different methods for creating electromagnetically induced structures have been discovered [3–12]. These all have a common element that instead of switching on and off a fixed structure, the structure is created by the electromagnetic field itself [13].

Probably the most noteworthy of these methods is that of the photorefractive effect [3]. Photorefractive materials are both photoconductive and electro-optic, Through the photoconductive effect donors or acceptors are excited from the band gap, where they are free to drift or be driven away. In this way a spatial arrangement of charge can accumulate in the darker regions that will modify the refractive index of the material through the electro-optic effect. Although this effect can be detrimental, such as in Electro-Optic Modulators, it may also be put to good use, such as in holographic recording [3] and electro-holographic switching [14]. While the induced photorefractive effect remains after the initial electromagnetic field ceases, many other systems have a much shorter lived response. These invariably involve using an atomic vapor to mediate the light matter interaction.

Included in these mechanisms is atomic optical pumping [4,5], where the incident light will excite the electrons in a resonant transition, allowing them to decay to a non resonant ground state, thus changing the number of atoms involved in a particular transition and correspondingly the resulting susceptibility.

Another way involves using non-linear susceptibilities to enhance phase conjugation and four wave mixing [6]. Coherent population trapping of atoms may also be used to enhance the FWM [8].

A different scheme involves the Faraday effect. Here right and left circularly polarized light interact with different Zeeman sub levels of the ground state. Normally these levels are degenerate, but in the presence of a magnetic field this degeneracy is lifted and Faraday rotation can occur, with the different polarizations experiencing different refractive indicies. A non-linear effect such as "hole burning" causes the non-linear Faraday effect, which can be orders of magnitude larger than the linear regime. Using this effect a grating based upon the control intensity can be created [7, 15].

It has also been shown theoretically and experimentally that creating a grating in the pump

laser in Electromagnetically Induced Transparency will cause diffraction to the probe, which can be used for optical routing [9–11]. In a different set-up a more general coherent Raman process has been shown to produce wave guiding [12].

It is the aim of this thesis to present and demonstrate a novel means of refractive index control using the AC Stark Effect. This concept is an extension of the double lorentzian atomic prism [16] where an increased atomic density is used to control the refractive index of an atomic vapor. In this work the essential idea is to manipulate this refractive index profile using a control laser, which shifts the transition lines through the AC Stark effect. Hence the most obvious realization of this is in an atomic vapor, such as of the alkali metals, such as rubidium and caesium. However one could envision other systems such as quantum dots or rare earth doped crystals where the same principles could apply. In contrast to previous methods, this is a non-resonant, incoherent process, that can work in systems even at high temperatures. Uses may be found in beam amplification, interferometry, optical interconnections [7] and control of quantum pulses.

The following section, "2 Theory", presents the basic theory behind this scheme to implement refractive index control through the AC Stark effect. This is followed by "3 Calculations and Experimental Design", which discusses the results of calculations and subsequent experimental design. "4 Results & Analysis" shows experimental results that demonstrate the use of this effect to cause diffraction as well as other behaviors of the system. Finally in "5 Conclusions & Discussion" the main conclusions are drawn and directions for further research are suggested.

2 Theory

This section starts by presenting the basic classical theory for atomic susceptibility due to an atomic transition. Then the corresponding result is presented from a quantized two level system by considering the steady state response to a dipole interaction. The dressed states are then introduced and it is shown that these cause an intuitive shift in frequency of the susceptibility. In order to connect to real systems, some features of multilevel systems and the most relevant properties of rubidium are discussed.

2.1 Atomic Transitions and Refractive Index,

A simple classical model of an atom can consider an atomic transition to be a damped harmonic oscillator [17]. Where the electron of charge, e, and mass, m, and an optical transition $\omega_0$with decay γ, is driven by an external electric field E(t).

$$\frac{d^2x}{dt^2} + \gamma\frac{dx}{dt} + \omega_0^2 x = -\frac{e}{m}E(t) \tag{2.1}$$

If the atom is driven by a sinusoidal field at ω, $E(t) = E\exp(i\omega t)$, then the atomic polarization is

$$p = \frac{e^2 E\exp(i\omega t)}{m(\omega_0^2 - \omega^2 + i\gamma\omega)} \tag{2.2}$$

and the susceptibility of the atom χ_a , defined as $\chi_a \equiv \frac{p}{\varepsilon_0 E}$, is

$$\chi_a(\omega) = \frac{e^2}{m\varepsilon_0(\omega_0^2 - \omega^2 + i\gamma\omega)} \tag{2.3}$$

Therefore for $\omega \approx \omega_0$

$$\chi_a(\omega) = \frac{e^2}{2\omega_0 m\varepsilon_0(\omega_0 - \omega + i\gamma/2)} \tag{2.4}$$

In a simplified picture the susceptibility of the gas, χ, will be a combination of the individual atomic susceptibilities convolved with the velocity distribution of the atoms, giving a Voight profile [17] (Doppler broadening is the dominant broadening mechanism in the regime of this thesis), which is then multiplied by the particle density, N (which is a function of temperature, N(T) subsection 2.6). A more correct expression involves other dephasing mechanisms that can be incorporated into the the decay rate [17].

This simplified model can be related to the refractive index of the media, n by

$$n^2(\omega) = 1+\chi(\omega) = 1+N(\mathrm{T})\,D_N\int \frac{e^2}{2\omega_0 m\varepsilon_0(\omega_0 - \omega' + i\gamma/2)}\times exp\left(-4ln2\left(\frac{\omega-\omega_0}{\Delta\omega_d}\right)^2\right)d\omega' \tag{2.5}$$

where the Doppler width, $\Delta\omega_d$, is given by

$$\triangle\omega_d = \sqrt{\frac{(8\ln 2)\,\mathrm{k_B T}}{\mathrm{mc}^2}}\omega_0 \tag{2.6}$$

and $\mathrm{D_N}$ is a normalization constant for the Doppler distribution given by

$$D_N = \sqrt{\frac{4\ln 2}{\pi\triangle\omega_d^2}} \tag{2.7}$$

2.2 Susceptibility in a Quantum Framework

To describe the susceptibility in a quantum framework the treatment of references [18,19] is followed. Treating the atom as a two level system with energies $\mathrm{E_1}$and $\mathrm{E_2}$, gives a bare Hamiltonian $\hat{\mathrm{H}}_0$,

$$\hat{\mathrm{H}}_0 = \begin{pmatrix} \mathrm{E_1} & 0 \\ 0 & \mathrm{E_2} \end{pmatrix} \tag{2.8}$$

which is perturbed by an electric field of a weak probe $\underline{\mathrm{E}}_\mathrm{p}(\mathrm{t})$ through a dipole interaction, $-\underline{\mu}\cdot\underline{\mathrm{E}}_\mathrm{p}$, and therefore perturbation $\hat{\mathrm{V}}(t)$

$$\hat{\mathrm{V}}(\mathrm{t}) = \begin{pmatrix} 0 & -\underline{\mu}\cdot\underline{\mathrm{E}}_\mathrm{p} \\ -\underline{\mu}\cdot\underline{\mathrm{E}}_\mathrm{p} & 0 \end{pmatrix} \tag{2.9}$$

thus the total Hamiltonian $\hat{\mathrm{H}}$ is

$$\hat{\mathrm{H}} = \hat{\mathrm{H}}_0 + \hat{\mathrm{V}} = \begin{pmatrix} \mathrm{E_1} & -\underline{\mu}\cdot\underline{\mathrm{E}}_\mathrm{p} \\ -\underline{\mu}\cdot\underline{\mathrm{E}}_\mathrm{p}^* & \mathrm{E_2} \end{pmatrix} \tag{2.10}$$

the density matrix of an ensemble of atoms, $\rho = \begin{pmatrix} \rho_{11} & \rho_{12} \\ \rho_{21} & \rho_{22} \end{pmatrix}$, will propagate in time as [20]

$$\dot{\rho} = -\frac{i}{\hbar}\left[\hat{H},\hat{\rho}\right] = -\frac{i}{\hbar}\left[\hat{H}\hat{\rho} - \hat{\rho}\hat{H}\right] \tag{2.11}$$

$$\dot{\rho} = -\frac{i}{\hbar}\begin{pmatrix} -\underline{\mu}\cdot\underline{\mathrm{E}}_\mathrm{p}(\rho_{21}-\rho_{12}) & (E_1-E_2)\rho_{12} + \underline{\mu}\cdot\underline{\mathrm{E}}_\mathrm{p}(\rho_{11}-\rho_{22}) \\ (E_2-E_1)\rho_{21} - \underline{\mu}\cdot\underline{\mathrm{E}}_\mathrm{p}(\rho_{11}-\rho_{22}) & -\underline{\mu}\cdot\underline{\mathrm{E}}_\mathrm{p}(\rho_{12}-\rho_{21}) \end{pmatrix} \tag{2.12}$$

Adding phenomenological damping with a decay time $\mathrm{T_1}$ for the excited state and decay time $\mathrm{T_2}$ for the coherence, and defining the transition frequency as $\omega_{12} \equiv \frac{\mathrm{E_1}-\mathrm{E_2}}{\hbar}$ will give the familiar optical Bloch equations

$$\dot{\rho_{11}} = i\frac{\underline{\mu}\cdot\underline{\mathrm{E}}_\mathrm{p}}{\hbar}(\rho_{21}-\rho_{12}) - \frac{\rho_{11}}{\mathrm{T_1}} \tag{2.13}$$

$$\dot{\rho_{22}} = i\frac{\underline{\mu}\cdot\underline{\mathrm{E}}_{\mathrm{p}}}{\hbar}(\rho_{12}-\rho_{21}) + \frac{\rho_{11}}{\mathrm{T}_1} \tag{2.14}$$

$$\dot{\rho}_{12} = -\left(i\omega_{12} + \frac{1}{\mathrm{T}_2}\right)\rho_{12} - i\frac{\underline{\mu}\cdot\underline{\mathrm{E}}_{\mathrm{p}}}{\hbar}(\rho_{11}-\rho_{22}) \tag{2.15}$$

where the equations for the off axis elements are related through $\rho_{21} = \rho_{12}^*$.

To investigate the response at probe frequency, ω, means taking

$$\underline{\mathrm{E}}_p(t) = \frac{\underline{\mathrm{E}}_p}{2}\left(e^{i\omega t} + e^{-i\omega t}\right)$$

and using the rotating wave approximation implies that

$$\underline{\mathrm{E}}_p(t) \cong \frac{\underline{\mathrm{E}}_p}{2}e^{-i\omega t}$$

.

Introducing the rotating frame $\sigma_{12} = \rho_{12}\exp(-i\omega t)$ gives

$$\frac{\mathrm{d}(\sigma_{12})}{\mathrm{dt}} = \left[i(\omega-\omega_{12}) - \frac{1}{\mathrm{T}_2}\right]\sigma_{12} - i\frac{\underline{\mathrm{E}}_p\cdot\underline{\mu}}{2\hbar}(\rho_{11}-\rho_{22}) \tag{2.16}$$

Taking the steady state solution in the limit of a perturbative probe, $(\rho_{11}-\rho_{22}) \to -1$, gives

$$\sigma_{12} = \frac{\underline{\mathrm{E}}_p\cdot\underline{\mu}(\rho_{11}-\rho_{22})}{2\hbar(\omega-\omega_{12}) + {}^{i}/_{\mathrm{T}_2}} \tag{2.17}$$

Substituting back in for $\rho_{12}$and finding the expectation value of the polarization

$$P(t) = \mathrm{N}\left\langle\hat{\mu}\right\rangle = \mathrm{NTr}(\hat{\rho}\hat{\mu}) = \mathrm{N}(\rho_{12}\mu_{21} + \rho_{21}\mu_{12})$$

and using the identities that $P(t) = Pe^{-i\omega t} + c.c$ and $P = \varepsilon_0\chi E$, the susceptibility is given by

$$\chi = \frac{\mathrm{N}\mu^2}{2\epsilon_0\hbar(\omega-\omega_{12}+{}^{i}/_{\mathrm{T}_2})} \tag{2.18}$$

A quantum version of equation 2.4 where a connection between the prefactors can be found by considering the energy radiated from a dipole [1,21]. The energy of an emitted photon will be equal to the energy of the oscillator

$$\hbar\omega = m\omega^2\left\langle r(t)^2\right\rangle \tag{2.19}$$

However the dipole the dipole μ is just er , and therefore

$$\Rightarrow \left\langle\mu\right\rangle^2 = e^2\left\langle r(t)^2\right\rangle = \frac{\hbar e^2}{m\omega} \tag{2.20}$$

2.3 The Dressed State and AC Stark Shift

The non-resonant AC Stark shift will be derived by considering the dressed states. This method is chosen for two reasons, firstly it is the most accurate for a system where the control and probe will be interacting with the same ground and excited levels [22, 23], secondly it will aid in later discussions.

Considering the atomic transition at frequency $\omega_0 = \frac{E_2 - E_1}{\hbar}$ as a two level system driven by a control field detuned from the transition by $\triangle_c = \omega_c - \omega_0$, and Rabi frequency $\Omega_c = \frac{\underline{E} \cdot \underline{\mu}}{\hbar}$, where $\underline{\mu}$ is the dipole of the transition, the following Hamiltonian is obtained

$$\hat{\mathrm{H}} = \hbar \begin{pmatrix} 0 & \Omega_c \cos((\omega_0 + \triangle_c)\, t) \\ \Omega_c \cos\left((\omega_0 + \triangle_c)\mathrm{t}\right) & \omega_0 \end{pmatrix} \tag{2.21}$$

acting on the state $\begin{pmatrix} |g\rangle \\ |e\rangle \end{pmatrix}$. In the Rotating frame, at ω_c, and with the Rotating Wave Approximation the Hamiltonian becomes

$$\hat{\mathrm{H}} = \hbar \begin{pmatrix} 0 & \Omega/2 \\ \Omega^*/2 & -\triangle_c \end{pmatrix} \tag{2.22}$$

the eigenvalues of this Hamiltonian are

$$\lambda_{\pm} = -\frac{1}{2}\Delta_c \pm \frac{1}{2}\sqrt{\Delta_c^2 + \Omega_c^2} \tag{2.23}$$

The new energy level, $\hbar\omega' = \hbar(\omega_0 + \triangle\omega_0)$, will be

$$\omega' = \omega_c - \sqrt{\Delta_c^2 + \Omega_c^2} \tag{2.24}$$

or alternatively the effective shift to the transition frequency $\triangle\omega_0$

$$\Delta\omega_0 = \Delta_c - \sqrt{\Delta_c^2 + |\ \Omega\ |^2} \simeq -\frac{|\ \Omega\ |^2}{2\Delta_c} \propto \frac{\text{Intensity}}{\text{Detuning}} \tag{2.25}$$

Due to the fact that the AC Stark effect works through a virtual photon it can be a very fast process, on the order of the detuning Δ_c of the control field ($\triangle \mathrm{E} \triangle \mathrm{t} \geq 1$. the energy of the virtual photon will be of the order of magnitude of the detuning of the control laser $\hbar\triangle_c$ giving a timescale of $1/\triangle_c$).

The eigenstates of the dressed Hamiltonian will be a combinations of the original eigenstates [24, 25]

$$|e'\rangle = \cos\theta\,|e\rangle + \sin\theta\,|g\rangle \tag{2.26}$$

$$|g'\rangle = -\sin\theta\,|e\rangle + \cos\theta\,|g\rangle \tag{2.27}$$

and mixing angle, θ, defined by

$$\tan 2\theta = -\frac{\Omega_c}{\Delta_c} \tag{2.28}$$

2.4 AC Stark Shift of Refractive Index

The central idea in this thesis is that it is possible to combine the previous phenomena in subsections 2.2 and 2.3 whilst the control is sufficiently detuned to avoid multilevel effects, subsection 2.5.

In essence equation 2.10 will become

$$\hat{H} = \hat{H}_0 + \hat{V}_s + \hat{V}_p \tag{2.29}$$

where $\hat{V}_s$ is the AC Stark perturbation from the control laser and $\hat{V}_p$ is the perturbation of the probe laser. In order to find the susceptibility of the probe for a Stark shifted system consider

$$\hat{H}_s = \hat{H}_0 + \hat{V}_s \tag{2.30}$$

which is from subsection 2.3 approximated by

$$\hat{H}_s = \hbar \begin{pmatrix} 0 & 0 \\ 0 & \omega_0 + \Delta\omega_0 \end{pmatrix} \tag{2.31}$$

with the shifted energy found in the Rotating Wave Approximation, equation2.24. Following the procedure of sub-section 2.2 will give the atomic Stark shifted susceptibility χ_s

$$\chi_s = \frac{\mathrm{N}\mu^2}{\epsilon_0\hbar(\omega - (\omega_0 + \triangle\omega_0) + {}^{i}/_{\mathrm{T}_2})} \tag{2.32}$$

It should be noted that this approximation assumes that the dipole operator and the decay constants remain unchanged even in the dressed state basis, which will cease to hold at larger mixing angles.

2.5 Saturation Effects and Optical Pumping

Considering equation 2.21 at large values of Ω_c and small detunings ($\Omega_c > \Delta_c$) aside from the Stark shifting there will be significant changes in the electronic populations of the atom, with a greatly increased probability of finding the electron in the excited level. With more than two levels, the electron will also decay out of the excited state to other energy levels, leading to optical pumping., see references [21,26]. The scattering rate for such a process is given by [27]

$$\mathrm{R_{sc}} = \left(\frac{\Gamma}{2}\right) \frac{({}^{\mathrm{I}}/_{\mathrm{I_{sat}}})}{\left(1 + 4\left({}^{\Delta_c}/_{\Gamma}\right)^2 + ({}^{\mathrm{I}}/_{\mathrm{I_{sat}}})\right)} \tag{2.33}$$

where $\Gamma = \frac{2\pi}{lifetime}$, $\mathrm{I} = \frac{1}{2}\mathrm{c}\varepsilon_0\mathrm{E_c^2}$ and $\mathrm{I_{sat}} = \frac{\mathrm{c}\varepsilon_0\Gamma^2}{4\Omega_\mathrm{c}^2}$

2.6 Rubidium

A practical implementation of the scheme outlined in subsection 2.4 requires a real system. For this rubidium the 37^{th} element was used which has two naturally occurring isotopes ^{87}Rb and ^{85}Rb. Rubidium has the advantage of a relatively simple electronic structure, with a single outer orbital electron, and has been very well studied for its uses in quantum optics and atomic cooling, and atomic clocks [27]. Another attractive feature of rubidium is its high vapor pressure, which changes greatly with temperature. This allows for density variations over many orders of magnitude with relatively small changes in temperature (from 25 ^{o}C to 130 ^{o}C the pressure changes from $10^{-7}$to 10^{-3} Torr). The atomic density may be calculated from the vapor pressure given by equation (1) in reference [27] and is shown in figure 2.1. Another practical advantage is that because of the wide uses of rubidium it is commercially available in standard quartz cells, (generally 7.5 cm long, 2.5 cm diameter) with optical grade windows. The contents may be natural abundance or isotopically pure.

In the D_1 transition of rubidium there are a total of 8 hyperfine transitions within an 8 GHz range, see figure 2.2a. In most of the presented work an isotopically pure ^{85}Rb was used for the experimental cell, giving four transitions, while the far-detuned frequency of the control laser was identified by the ^{87}Rb transitions (primarily the F=1$\rightarrow$F'=2 transition) in a natural abundance cell.

There is flexibility in choosing the frequencies of the control and probe lasers as it is sufficient for them to share a common level for the AC Stark scheme of subsection 2.4 to work. If the control and probe only share a common ground level then the shift will be half that of equation 2.25. The maximum shift will be when they share both the ground and excited levels, however this choice adds a challenge of designing an experiment that will separate the two lasers which will be nearly identical in frequency (separated by approximately the control detuning Δ, O(GHz)). In this work the frequencies used were all close to the ^{85}Rb D_1 lines (795 nm), with the AC Stark shift for one transition shown in Figure 2.2b.

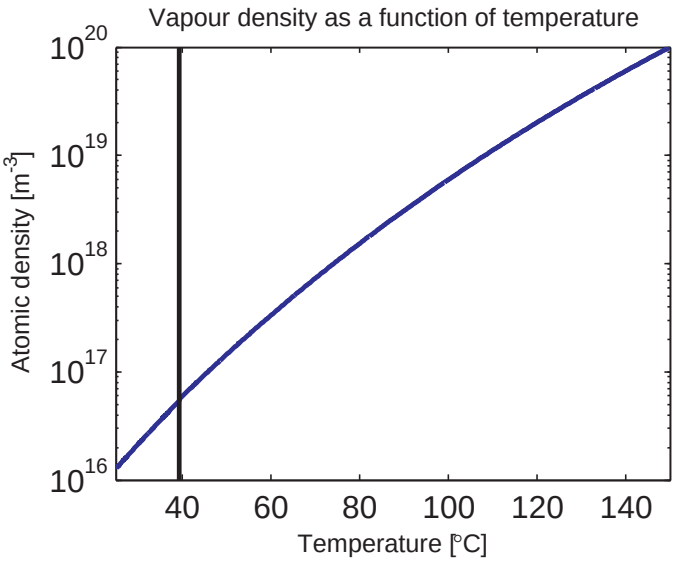

Figure 2.1: The change in vapor density of rubidium 85, based upon the empirical formula in reference [27]. The black line signifies the solid/liquid phase transition.

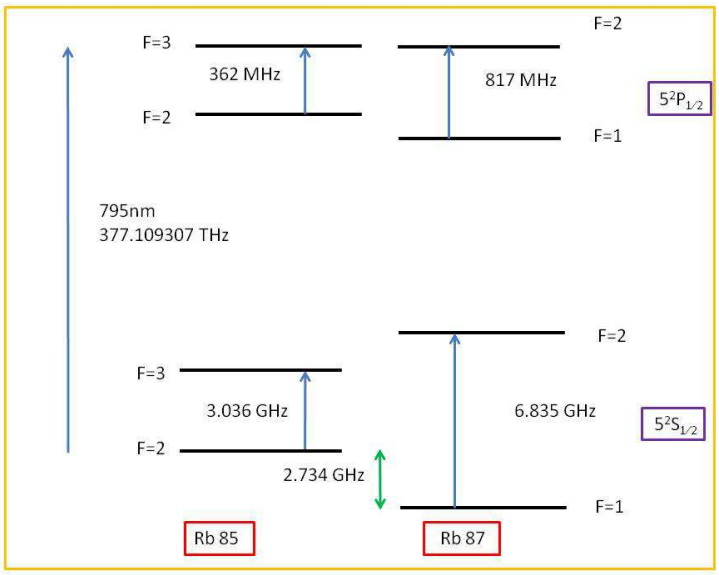

(a) Energy levels of the eight rubidium D_1 transitions.

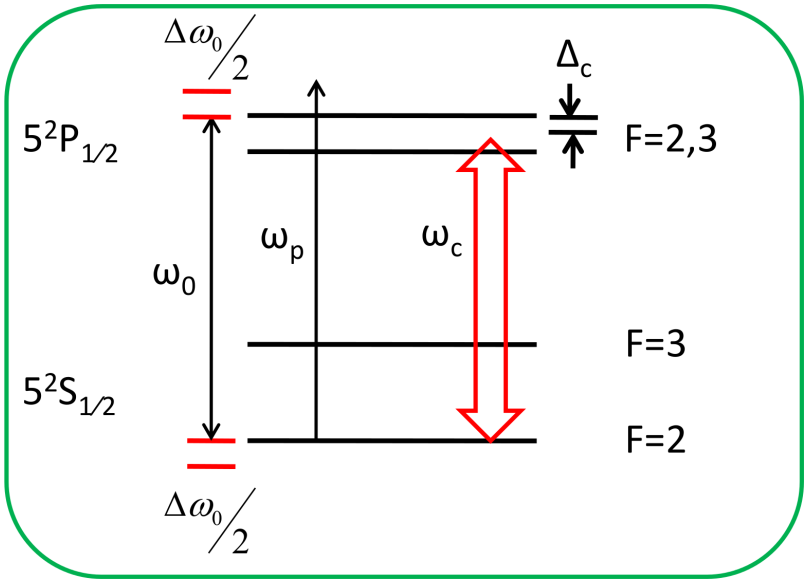

(b) AC Stark shifting of ^{85}Rb D_1 lines. A control laser detuned from a transition by Δ_c will cause a shift to each of the levels of a transition ω_0 of $\Delta\omega_0/2$. The probe at frequency ω_p experiences the transition with shifted frequency $\omega_0 + \Delta\omega_0$.

Figure 2.2: Rubidium D_1 transitions

3 Calculations and Experimental Design

This section presents the experimental design and begins with calculations of the expected change in refractive index, given the limitations of the available resources. This leads to an experimental design of a thick Bragg grating. Simulation results of the expected grating are presented that demonstrate design feasibility and appropriate parameters. Finally experimental details are discussed.

3.1 Calculations

The first step in determining the feasibility of implementing the concept described in sub-section 2.4 was to calculate the expected refractive index contrast that could be achieved, with special regard to the available resources. This involved considering the practical limitations of the available control laser in terms of power ($\sim$ 100 mW) and focusing capabilities (f $>$ 4 cm). Furthermore there were constraints on heating the available Rubidium cell ($\sim$ 100 °C), both in terms of its ability to withstand the heating and the resulting increase in optical density. The question "how large a change in the refractive index can be expected?" needed to be answered whilst taking into consideration these constraints. The answer to this question began by calculating the susceptibility as in Equation 2.5 both with and without the expected AC Stark shift. This required finding the difference between two shifted Voight profiles [17], Figure 3.1a, where the shift was caused by the expected AC Stark shift. Of interest was the resulting change in the refractive index and absorption through the cell that would be the consequence of these profiles Figure 3.1b. If the un-shifted susceptibility is χ_0 and the AC Stark shifted susceptibility is χ_s, then the corresponding refractive indicies will be $n_0' + in_0'' = \sqrt{1+\chi_0}$ and $n_s' + in_s'' = \sqrt{1+\chi_s}$. Then the shift in the real part of the refractive index δn will be

$$\delta \mathrm{n} = \mathrm{n}_0' - \mathrm{n}_\mathrm{s}' \tag{3.1}$$

the absorption α_0 is

$$\alpha_0 = \frac{2\pi \mathrm{n}_0''}{\lambda} \tag{3.2}$$

and the shift in α, is $\delta\alpha$ where

$$\delta\alpha = \frac{2\pi\left(\mathrm{n}_0'' - \mathrm{n}_\mathrm{s}''\right)}{\lambda} \tag{3.3}$$

The transmission T_0 through a rubidium cell length L without any Stark shift will then be given by

$$\mathrm{T}_0 = \exp(-\alpha_0 \mathrm{L}) \tag{3.4}$$

By calculating these values, Figure 3.1b it was seen that a change in the real part of the refractive index of O(10^{-6}) could be achieved away from the center of a transition line, where there was still significant transmission O(20 - 80%). A larger change in the real part of refractive index of O(10^{-5}) would occur at the center of the transition but this is accompanied by a large imaginary part of the refractive index and hence negligible transmission.

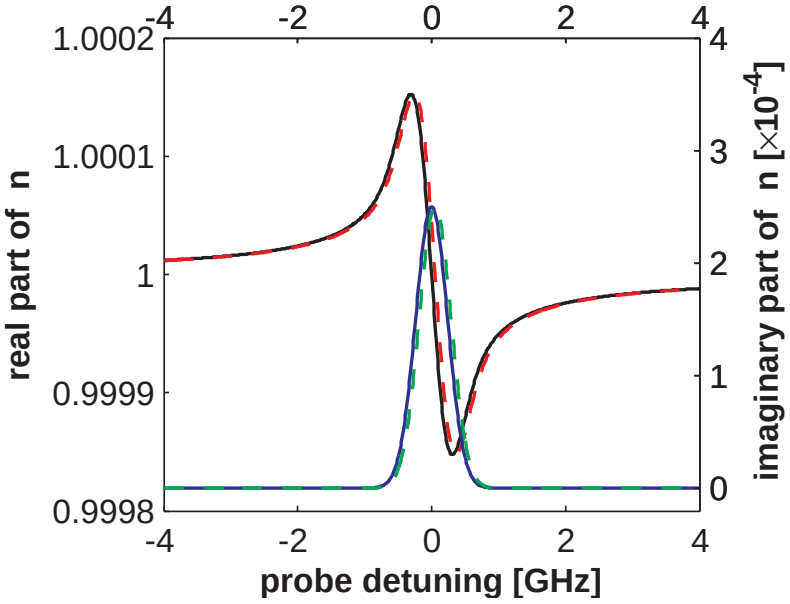

(a) Calculated shift in complex refractive index due to AC Stark, The bold lines show the unshifted refractive index of a rubidium transition (real part - black, imaginary - blue). The dashed lines show the refractive index in the presence of the control laser which induces an AC Stark shift that shifts the refractive index profile (real part - dashed red, imaginary - dashed green).

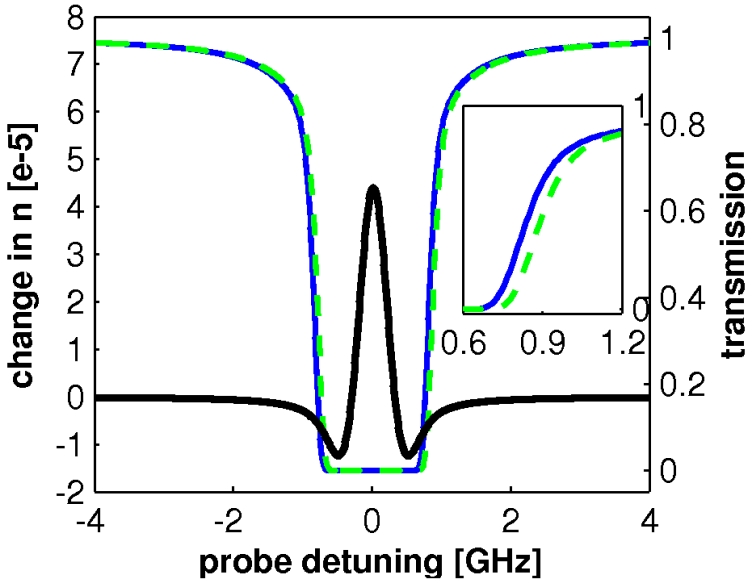

(b) The shift in the refractive index creates a contrast in both the real part of refractive index (black) and the imaginary part. The imaginary part causes absorption through the cell. The unshifted profile (solid blue) is shown contrasted to the shifted profile(dashed green).

Figure 3.1: Calculated shift in refractive index due to the AC Stark Effect. Laser power of 60 mW , waist size $800\mu m \times 85\mu m$, detuned by 2.7 GHz. The rubidium cell of 7.5 cm is heated to 85 °C. This calculation is for a single Doppler broadened transition.

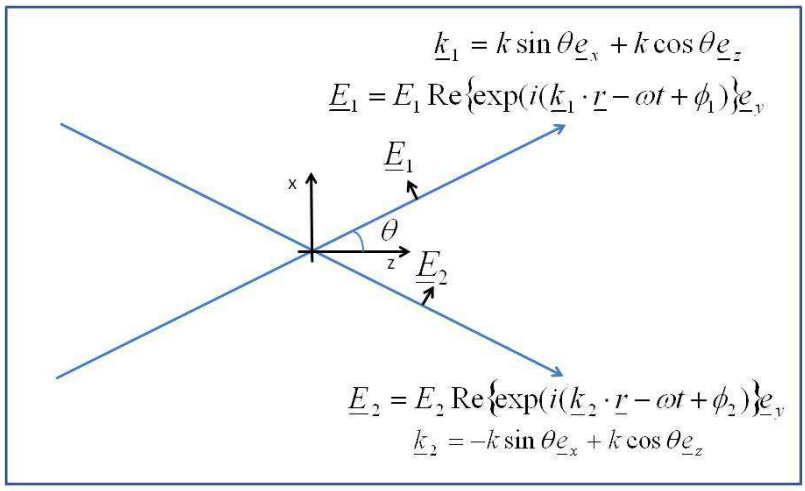

Figure 3.2: Two interfering electromagnetic fields

3.2 Experimental design

It was decided to build a thick Bragg grating [28] in order to detect the change in refractive index. This was chosen in order to use a periodic arrangement to combine together the predicted small phase shifts, $\delta n \approx 0(10^{-6})$. A thick Bragg grating has the property that light incident at the Bragg angle will be diffracted at the Bragg angle. In an ideal case (sufficiently thick), there will not be other orders of diffraction and the incident light can (theoretically) be completely diffracted into this order.

A thick Bragg grating can be made when two co-propagating coherent electromagnetic fields interfere, if the intensity profile is converted into a corresponding refractive index profile.

Two electric fields $\underline{E}_1$and $\underline{E}_2$ as in Figure 3.2 , assuming $|\underline{E}_1| = |\underline{E}_2|$and taking the polarization to be in the y direction gives an intensity

$$\begin{aligned} \mathrm{I} &\propto \left\langle |\underline{E}_1 + \underline{E}_2|^2 \right\rangle \\ &\propto \left\langle |\underline{E}_1|^2 \right\rangle + \left\langle |\underline{E}_2|^2 \right\rangle + 2\left\langle |\underline{E}_1 \cdot \underline{E}_2| \right\rangle \\ &\propto E^2 + E^2 \left\langle \cos\left(\underline{k}_1\cdot\underline{r} - 2\omega t + \underline{k}_2\cdot\underline{r} + \phi_1 + \phi_2\right) + \cos\left(\underline{k}_1\cdot\underline{r} - \underline{k}_2\cdot\underline{r} + \Delta\phi\right)\right\rangle \\ &\propto E^2 + E^2\cos\left(2k\sin\theta x + \Delta\phi\right) \end{aligned} \tag{3.5}$$

The intensity grating will therefore have spacing $d = \frac{\lambda_c}{2\sin\theta}$, however the Bragg angle is given by $\sin\theta_B = \frac{\lambda_p}{2d}$. Therefore when $\lambda_p \backsimeq \lambda_c$ such an intensity grating will have the property that the Bragg angle for the probe will be equal to the incident angle of the interfering control lasers.

Therefore for such intensity gratings, the diffracting probe needs to be aligned along one of the control beams, and then the resulting diffracted probe will then lie upon the other control beam.

It was decided to use a configuration of counter-propagating orthogonally linearly polarized beams, see Figure 3.3. This is because such a configuration will create a 'clean' port for the signal.

In discussion of this system, terminology that is specific to this system is defined in Table 1.

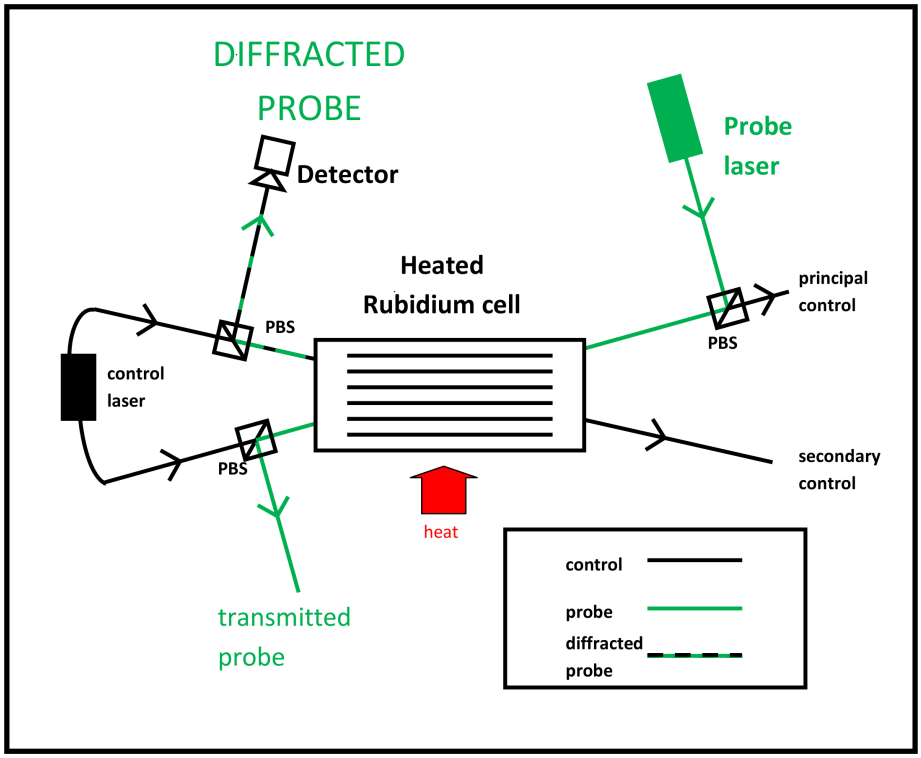

Figure 3.3: Schematic of experimental set up

name	definition
principal control	the beam upon which the transmitted probe lies
secondary control	the beam upon which the diffracted probe lies
transmitted probe	the probe that is not diffracted
diffracted probe	probe that has undergone diffraction

Table 1: Definition of terms

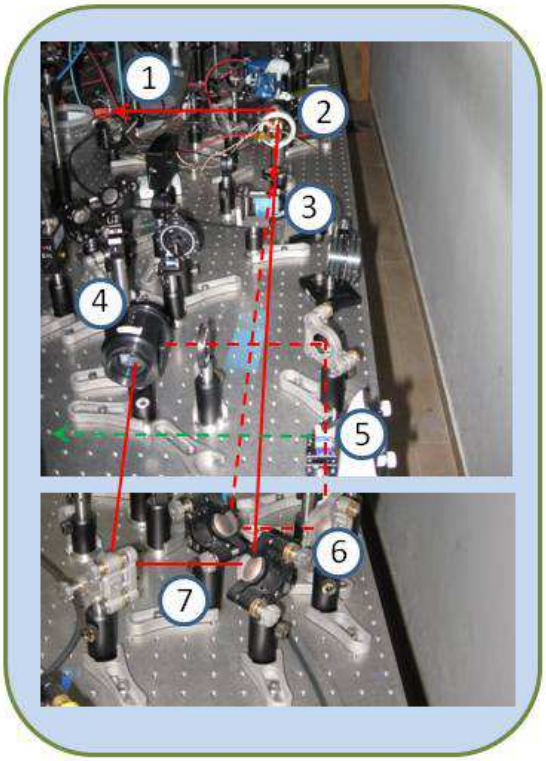

(a) 1 Continuation of control path, 2, Rubidium Cell, 3, Cylindrical lens f=30 cm in vertical direction, 4,NPBS - creating the two control beams, 5,PBS - to separate the diffracted probe (dashed green), 6, Two mirror walk for secondary control (dashed red), 7, Two mirror walk for principal control (red).

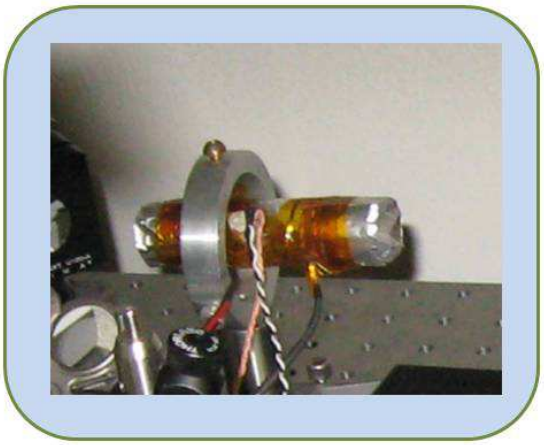

(b) Mounted Rubidium cell with heater, thermocouple and shielded windows

Figure 3.4: Photograph of the experimental set up

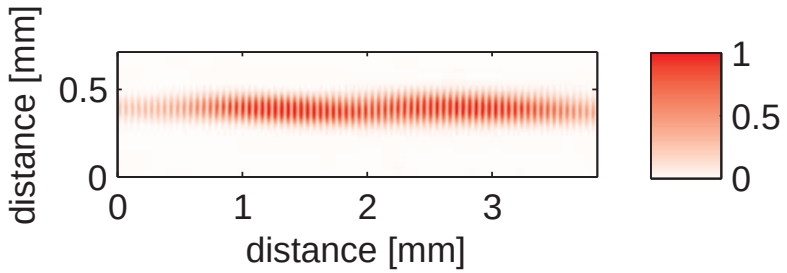

(a) Interference of two control beams, spacing 55 µm, height 150 µm, width ≈ 3 mm through the length (7.5 cm) of the cell

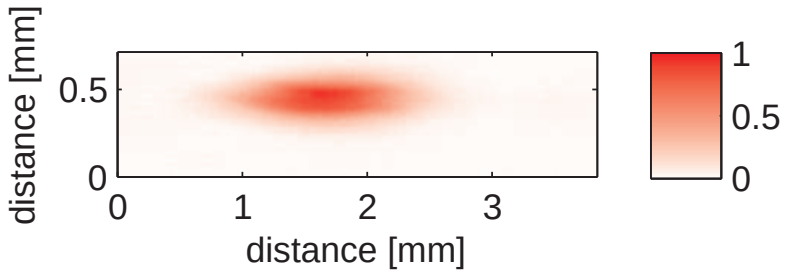

(a) Probe beam in middle of the cell , horizontal waist 615 µm vertical waist 155 µm

Figure 3.5: The interfering light beams are translated into a refractive index grating through the length of the rubidium which causes diffraction of the probe

3.3 Simulation

Simulations of the expected response of this interference grating were carried out in order to determine if the grating could produce a detectable response. Although the theoretical efficiency of a thick Bragg grating can be 100%, this is only in an ideal case, and for well defined grating lengths and angles. In the proposed grating produced by two interfering Gaussian beams there will be an envelope in refractive index that follows the intensity of the interfering laser beams. The grating efficiency will also be determined by the fixed cell length and the deviation of the probe from the Bragg angle. Thus a simulation of a probe propagating through space with a spatially dependent phase difference, corresponding to the intensity of the control, was carried out to determine the feasibility of this experiment.

Initially it was assumed that the absorption would give an overall attenuation to the diffracted signal. However in later simulations more detail was added by including both parts of the refractive index, as well as using a more accurate expression for calculating the susceptibility (see appendix 6.1). Initial calculations showed an expected change in refractive index of the order of 10^{-6}.

In the simulation the grating region was modeled by adding a spatially dependent phase

$$\phi(x,y,z) = \frac{2\pi}{\lambda}\delta n I(x,y,z)z + i(\alpha + \delta\alpha_0 I(x,y,z))z \tag{3.6}$$

From the calculations and simulations, figure 3.6, it could be seen that a diffracted signal of O(1 μW), starting with a probe power of 1 mW, could be achieved with the rubidium cell heated to around 100°C, and a control laser power of 100 mW, detuned by 2 GHz from a transition, and interfering with an angle between the control beams of 0.01 rad, all realistic experimental parameters.

It was also possible to see various ways to improve the grating efficiency. Figure 3.7a showed the importance of a small interference angle and good alignment. Figure 3.7b showed the importance of matching the probe size to the grating. While Figure 3.7c showed the importance of achieving a large change in refractive index contrast, δn.

For an AC Stark grating, it was expected that for small values of the refractive index contrast, δn, and large detunings of the control laser that equations 2.25 and 3.1, could be linked giving,

$$\delta n \propto \delta\chi \propto \frac{\partial\chi}{\partial\omega}\delta\omega \propto \frac{Intensity}{Detuning} \tag{3.7}$$

Using the result, for small values of δn, the efficiency will be proportional to $(\delta n)^2$ [28], it was expected that the efficiency of the grating, e, would be related to the Stark shift by,

$$e[\%] \propto (\delta n)^2 \propto \left(\frac{Intensity}{Detuning}\right)^2 \tag{3.8}$$

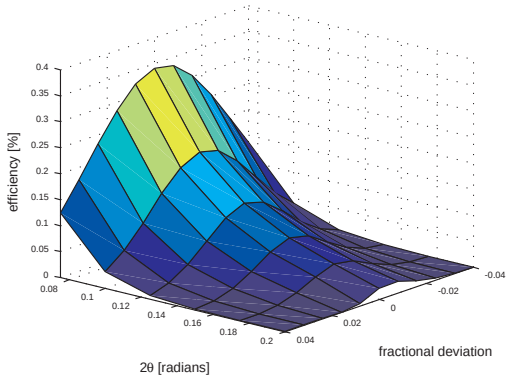

(a) Expected grating efficiency versus angle between control beams, 2θ, and probe fractional deviation from Bragg angle, $\frac{\Delta\theta_{probe}}{\theta_{Bragg}}$, with equally sized probe and control beams, and with refractive index contrast $\delta n = 10^{-6}$, .

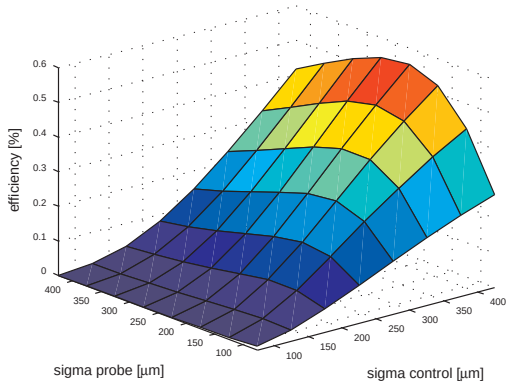

(b) Expected grating diffraction efficiency versus control and probe sizes, with perfect alignment, $2\theta = 0.01$ rad, and with refractive index contrast $\delta n = 10^{-6}$.

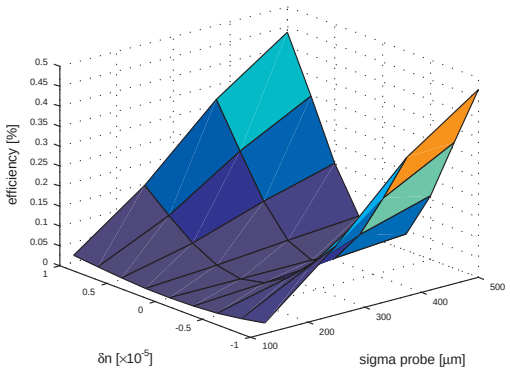

(c) Expected grating efficiency with changing probe size and refractive index contrast.

Figure 3.6: Simulations of the expected grating efficiency , show that an efficiency of O(0.1%) can be achieved with an angle between the control laser beams of 0.01 rad and equal control and probe beam sizes. Increasing the δn will increase the efficiency.

3.4 Experimental methods

Rubidium cell

For the majority of results presented the grating was created in an isotopically pure ^{85}Rb cell, (diameter 2.5 cm, length 7.5cm) with no buffer gas, however this was unavailable for the time domain experiments and so in these experiments a cell of natural abundance Rubidium (78% ^{85}Rb and 22% ^{87}Rb) with no buffer gas was used. An isotopically pure cell enabled identification of the control laser detuning with minimal absorption in the experimental cell. This was achieved by tuning the control laser to a ^{87}Rb D_1transition and observing the diffracted signal on the ^{85}Rb D_1lines. In a natural abundance cell at high temperatures a large amount of absorption of the control laser occurred in this arrangement.

Scanning and identifying the laser frequencies

The probe laser was a Distributed Feedback Laser (Toptica DL 100) and had very good stability in time (with negligible drift in the course of an experiment) and with a large mode hop free range (20 GHz). The frequency was measured by saturation absorption spectroscopy (using a Toptica CoSy system) [29].

The control laser was a home built External Cavity Diode Laser with a grating in the Littrow configuration [30] . The mode hop free range was much smaller (up to 3 GHz, typically less than 1 GHz). The frequency was adjusted by altering the current, and temperature of the diode, and through a piezo electric crystal attached to the back of the grating. The frequency was measured by saturation spectroscopy (an in-house set-up).

The limited mode hop free range of the ECDL presented a problem in measuring large detunings of the laser ($>$ 2 GHz). Measurement of detunings outside of the absorption lines was accomplished by making small changes in the current (of the laser diode) and dc offset voltages (of the grating piezo electric crystal). These adjustments caused a small shift in the center of the location of the frequency scan of the laser. By keeping the shifts small so that an overlapping frequency region was scanned each time, and under the assumption that the frequency scanning was linear and did not change as the stable region moved the frequency was scanned and results of Figure 4.4 were obtained. Using this method it was possible to obtain a scan of over 12 GHz. This method was used several times with similar results.

Temperature control

Temperature control of the cell was achieved by wrapping the rubidium cell in about eight loops of Nikrothal 60 (a NiCr alloy). A maximum power of approximatetly 30 W was used to heat the cell. The temperature was monitored using a thermistor (Thorlabs TH10K). The thermistor was attached close to the cold spot of the cell to give the best measure of the vapor density.

Time modulation

For time modulation of the signal the results presented are from modulations with an Electro-Optic Modulator. An EOM (100 MHz Phase Modulator: Thorlabs E0-PM-NR-C1) was added to the control beam path (before it was split by a non polarizing beam splitter - to give greater contrast). Amplitude modulation was achieved by addition of a polarizer to the path after the modulator. Maximization of the amplitude modulation was achieved by addition of both $\lambda/2$ and $\lambda/4$ wave plates to the path of the light. This provided compensation to 'align' the crystal axis with the polarizer and adjust for thermal phase drift due to the uncompensated crystal in the phase modulator. The electric field was an amplified (PHILPIS BGD902) output from a signal generator. Amplitude modulations of up to 20% at frequencies ranging from 2 MHz to 800 MHz (a combination of the limitations of the bandwidth of the EOM and the amplifier) were obtained. Additionally a 'smart switch' (consisting of a polarizing cube and $\lambda/2$ wave plate) was added to the diffracted probe path. This enabled the signal to be switched to a 'fast' amplified 8 GHz bandwidth detector (Thorlabs PDA8GS) after being aligned using a 'slow' detector (Thorlabs DET10A & Thorlabs PDA36A). The small modulation signal of the diffracted probe was measured on a spectrum analyzer (Agilent N9010A).

Power variations

The power of the probe and control was varied using a waveplate ($\lambda/2$) in a rotation mount before a polarizer. The transmitted power for a specific phase plate rotation was calibrated by measuring the transmitted power on a power meter.

3.5 Building the experiment

The control laser was split by a Non Polarizing Beam Splitter in order to create two paths, named the "principal control"and the "secondary control" figure 3.4 and table 1. Care was taken to ensure that the path length of each branch remained equal (for time domain experiments). A two mirror walk was added to each control path for the purpose of alignment and grating adjustment. The angle between the principal and secondary control was measured and adjusted by observing the spacing of the grating on a camera. The axis of the principal control was aligned first and kept fixed with other directions and angles being aligned relative to this direction. The resulting control inteference, and probe can be seen in Figure 3.5.

3.6 The signal

The experimental design gives a clean port for the diffracted signal, but this creates a difficulty in locating the exact location of this signal. Locating the signal was accomplished by firstly adjusting the part of the secondary control that was reflected inside the PBS, this was reflected back along itself. Then the portion of the secondary control that was reflected inside the polarizing cube onto the expected path of the diffracted probe, was used as a guide for the correct location of the

expected diffracted signal. The control laser was then tuned to a ^{85}Rb D_1 resonance to create an optical pumping grating and the location was optimized with this diffracted signal. Care was taken not to amplify the background signals that reached the diffracted probe path. These consisted of a portion of the control laser that was reflected inside the PBS and part of the transmitted probe that was clipped by the mirror on the secondary control path.

4 Results, Analysis & Discussion

This section presents the main results of the electromagnetically induced grating. In the first subsection, diffraction from the grating is demonstrated. The results of scanning the probe frequency verify that this grating is the result of the AC Stark effect. The next subsection shows results of scanning the control frequency, which also shows the grating efficiency decays in a way consistent with the AC Stark effect. The following subsection shows the results of changing the probe power, which gives an unexpected result of nearly constant efficiency. The next subsection shows the effect of changing the cell temperature, with an increase in efficiency with cell temperature. Following this the result of changing the control laser power is shown to be consistent with the AC Stark effect. The final subsection discusses some results of time response measurements, which do not show the expected fast response, reasons for this are suggested.

4.1 Main Result: Diffraction from an AC Stark Effect Grating

The first result was the detection of diffraction of the incident probe laser at the predicted Bragg angle. This was observed while scanning the frequency of the probe laser through the ^{85}Rb D_1 transitions, and keeping the control laser detuning constant. A diffracted probe signal was observed around the frequencies of the ^{85}Rb D_1 transitions at the expected locations, corresponding to the edges of the absorption, Figure 4.1. The diffracted signal was demonstrated to be due to the grating by the fact that it was only observed in the presence of both control beams and probe laser, blocking either control beam destroyed the diffracted signal. (This check was used in all experiments to verify that a true diffracted signal was being observed). The small background, in the absence of a grating, was derived from two sources. Firstly, a small amount of the secondary control entered the path of the diffracted probe, due to non ideal optical elements (especially as these were engineered for a wavelength of 780 nm and not 795 nm (which corresponds to the Rb D_1lines)). These imperfections caused a small fraction of the secondary control to be reflected within the polarizing beam splitter, PBS, and reached the diffracted probe detector. Secondly, due to the shallow angle ($<0.5^{\circ}$) between the control beams and hence transmitted and diffracted probes, a small fraction of the diverging probe was clipped by a mirror on the path of the secondary control and hence diffracted probe, which entered the detector for the diffracted probe.

This diffraction signal, Figures 4.1 and 4.2, (where the control was on the ^{87}RbF1 $\rightarrow$ F′2 transition) was clearly the result of a non-resonant AC Stark Effect as the control was detuned by 2.7 GHz from the closest ^{85}Rb transition. The optical pumping decays as $(1/\Delta)^2$ for large detunings, reference [27] , and was therefore negligible in this experiment. The fact that the signal appeared at the frequencies on the edge of the transmission signal where a significant change in refractive index, δn, was accompanied by significant transmission was consistent with the theoretical expectation, see Figure 3.1b. There was a peak on each side of the absorption profile, and the overall diffraction efficiency tended to decrease with increased detunings of the control laser (corresponding to a reduction in AC Stark effect, Equation 2.25). The relative heights of the different peaks can largely be explained by considering the absorption. In addition to the decrease in size with detuning, the AC Stark effect also caused a change to the imaginary part of the refractive index. This resulted in the signal corresponding to the closer side of the absorption occurring at a greater transmission, and hence greater efficiency, than the signal on the further side. The overall consistency between the simulation and the results with no fitting parameters, figure 4.2 provided further support for the understanding that the grating was produced by the AC Stark effect.

In order to understand the relative heights of the different peaks in the diffracted signal, calculations and simulations were done that included the different hyperfine transitions, their relative strengths and corresponding detunings, whilst including the effect of counter-propagating probe and control lasers, optical pumping and saturation effects, see Appendicies 6.1 and 6.2.

A better insight into the subtleties of the process was obtained by considering what happened when different effects were removed from the susceptibility calculation and simulation, Figure 4.3. The main effects were to consider the imaginary part of the refractive index, by including the

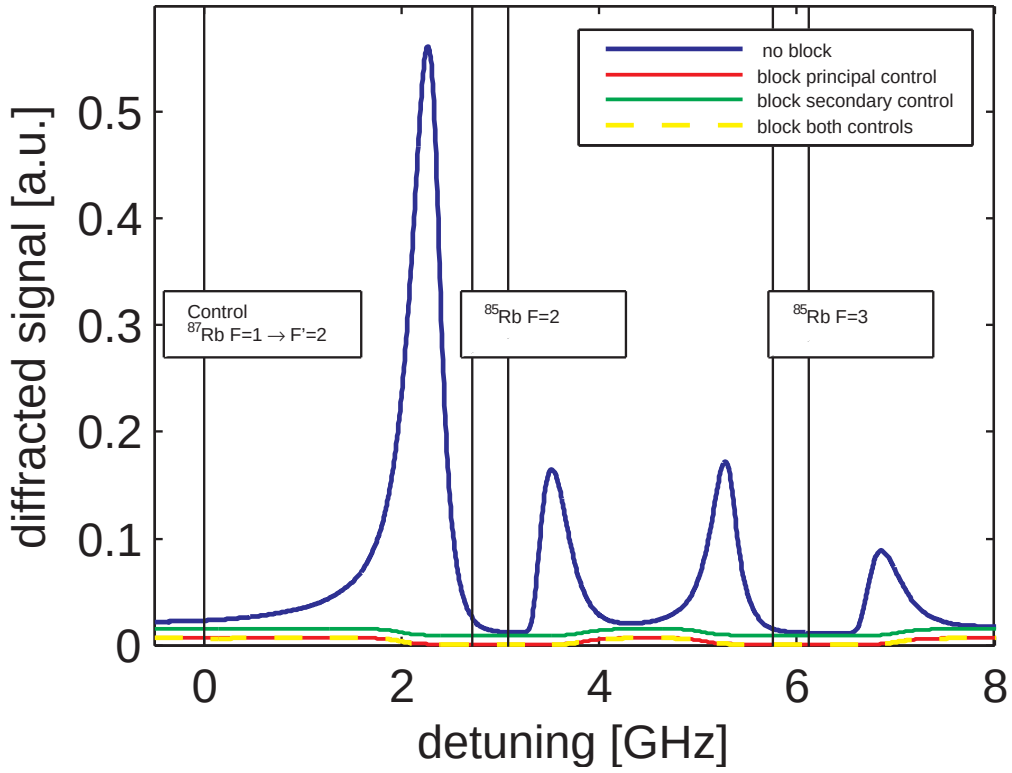

Figure 4.1: Diffracted signal with background. The detuning was measured from the ^{87}RbF1 $\rightarrow$ F′2 transition, where the control laser was positioned. [cell temperature = 135 ˚C, grating spacing = 55 µm, laser power = 50 mW].

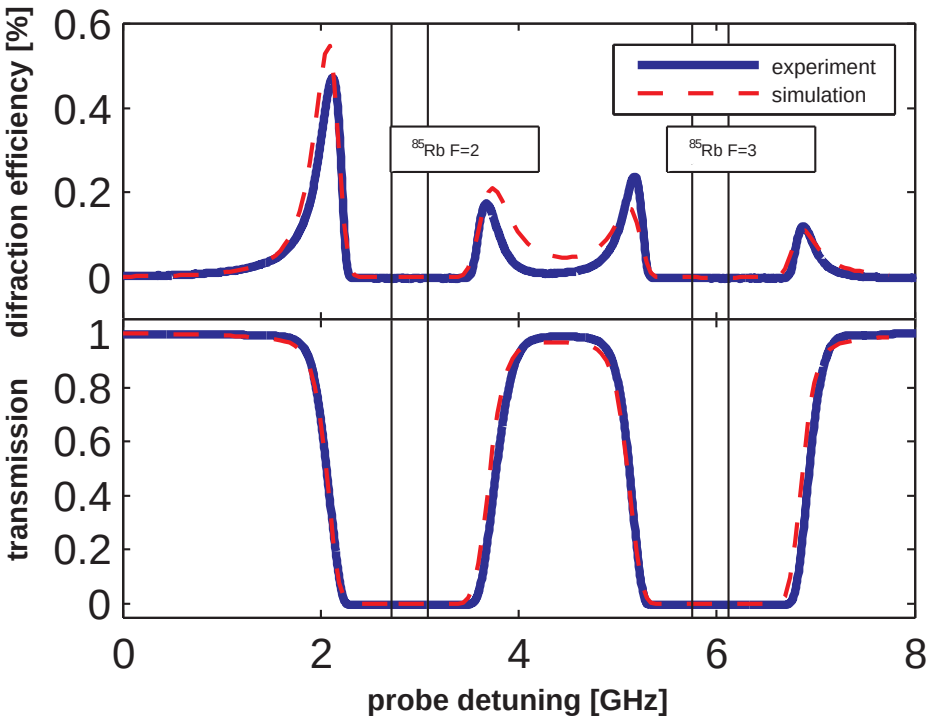

Figure 4.2: The probe detuning is scanned while the the control laser frequency is kept at constant frequency on the ^{87}Rb F $= 1 \rightarrow$ F$' = 2$ transition, the detunings were measured from this frequency. [cell temperature = 135 °C, grating spacing = 55 µm, laser power = 60 mW].

absorption coefficient, α, and a phenomenologically lower temperature for the number of atoms, calculated using Reference [27]. Removing the absorption coefficient, α, from the simulation (Figure 4.3a solid orange) showed where the absorption had a strong effect on the grating efficiency.

Using the measured temperature for the number of atoms , Figure 4.3a (solid green), showed a greatly increased diffraction efficiency which occurred at the edge of a broadened absorption profile, due to the increased change of the real part of the refractive index, δn, even though there was also increased absorption, which displaced the detuning of the maxima. The reason for this phenomenological temperature is believed to be due to optical pumping by the probe laser, which effectively reduces the number of atoms involved in the grating.

Smaller changes are caused by an absorption grating, a result of the relative differences in the absorption coefficient, $\delta\alpha$. Removing the effect of the absorption grating, Figure 4.3b (dashed green) decreased the diffraction efficiency and caused a shift in the signal away from the transition lines. Hole burning of the probe, Figure 4.3a (dashed orange), also caused a small shift in size and position of the signal, this could also be related to the optical pumping being stronger for atoms that are resonant with the probe laser.

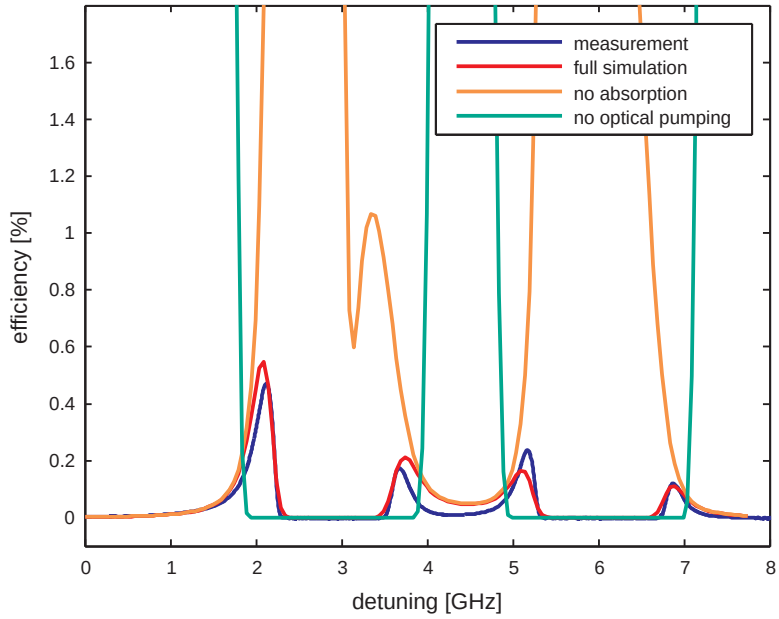

this

(a) Simulation with atomic density at measured temperature (135°C) instead of phenomenological temperature (75°C) (solid green), and without considering absorption (solid orange).

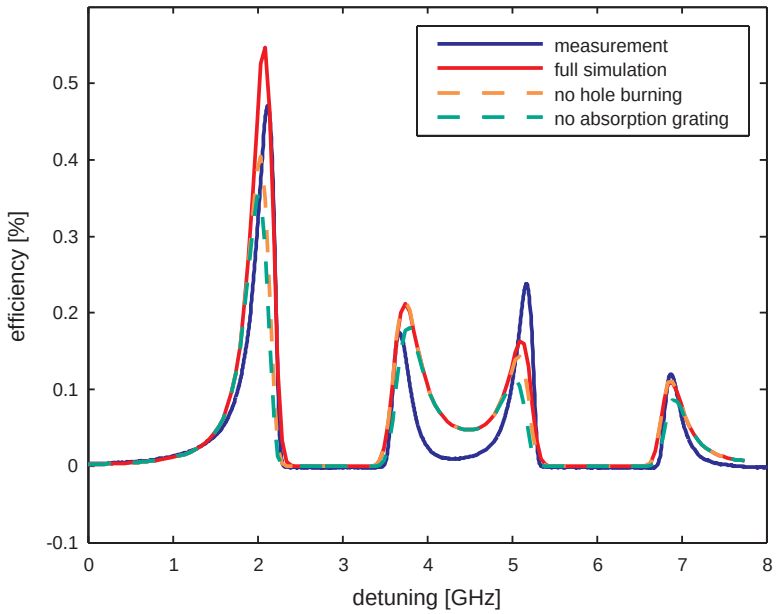

(b) Simulation without absorption grating (dashed green) and no hole burning (dashed orange).

Figure 4.3: The effects of changing parameters in susceptibility calculation and simulation. The measured signal (blue) and complete simulation (red) are shown in both figures

4.2 Control Laser Detuning

In a different experiment the control laser frequency was varied while the probe frequency was kept constant. It can be seen in Figure 4.4 that the diffraction efficiency fell off with increased detuning. Fitting to a logarithmic plot gave a fit of -1.99 ± 0.02. consistent with theoretical expectations for large detunings as in equation 3.8. When the control frequency came close to the ^{85}Rb F=2 lines, optical pumping increased and the efficiency of the grating decreased. When the control frequency was on the other side of the ^{85}Rb F=2 lines the AC Stark shift was in the opposite direction and the probe lay in a region of strong absorption and no diffraction was observed (at this probe frequency).

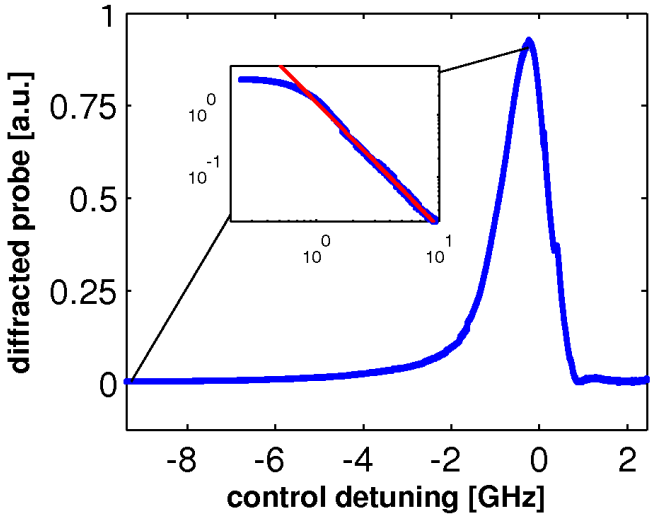

Figure 4.4: The control detuning was scanned while the probe detuning was kept constant (at 2.2 GHz from the ^{87}Rb F $= 1 \rightarrow$ F$' = 2$ transition the peak in 4.2). The sign of the detuning was chosen to be consistent with 4.2 (moving away from the ^{85}Rb D_1 transitions)

4.3 Probe Power

The probe power was scanned according to the method of subsection 3.4. It was seen that for larger probe power there was an increased diffraction signal, Figure 4.5a. At higher probe powers the maximum of diffraction occurred closer to the ^{85}Rb D_1 transitions. This was explained by the fact that the probe was not in a perturbative region. Even though a low probe power was used, the cylindrical lens caused an increase intensity and hence optical pumping and saturation effects. This led to an effective reduction of the the atomic population involved in the grating, as can be seen by the reduced absorption, Figure 4.6. Thus the change in frequency of the maxima can be understood that at higher probe powers and hence more optical pumping there is a lower effective density of atoms, allowing the diffracted signal to occur closer to the transition lines. Additionally diffraction can also be seen on the transition lines.

Although at higher probe powers there was the expected increase in diffraction this was not accompanied by an increase in the maximum grating efficiency, Figure 4.5b. This is somewhat surprising as it was expected that reducing the probe power would be roughly equivalent to increasing the temperature of the cell with an expected increase in the efficiency, sub-section 4.4. It is suggested that the increase of the saturation effects could be compensating (see subsection 4.1) for this reduction in density. Another surprising result is the difference between the F=2 and F=3 transitions, with a much greater change in optical density occurring on the F=2 transition, Figure 4.6.

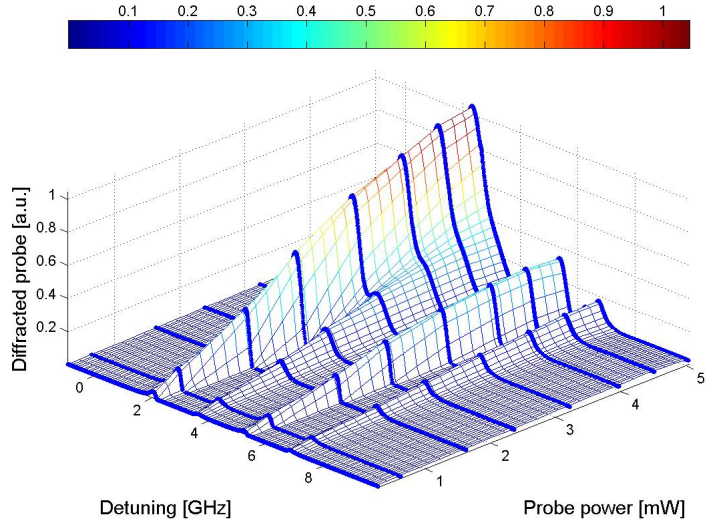

(a) Absolute power of diffracted probe

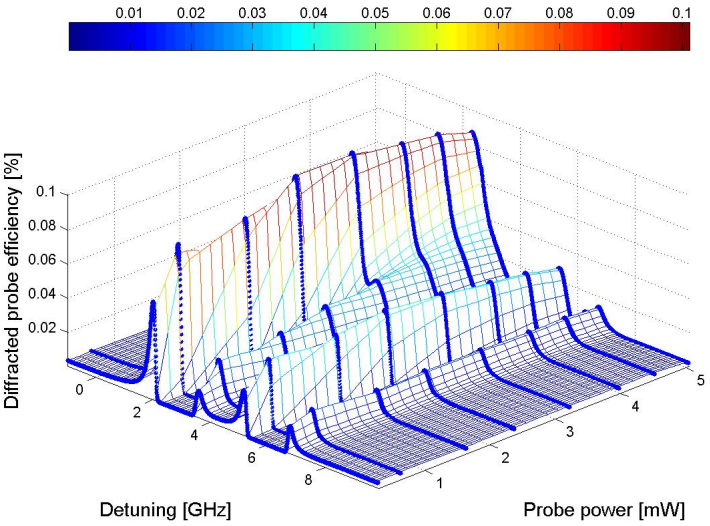

(b) Efficiency of diffracted probe

Figure 4.5: Probe power scan: diffraction. The diffraction probe signal when the probe frequency was scanned at different probe powers. cell temperature = 126°C, control 61mW on ^{87}Rb F=1 → F'=2 transition, grating spacing = 55 μm. The data points are shown in blue, with an interpolated grid

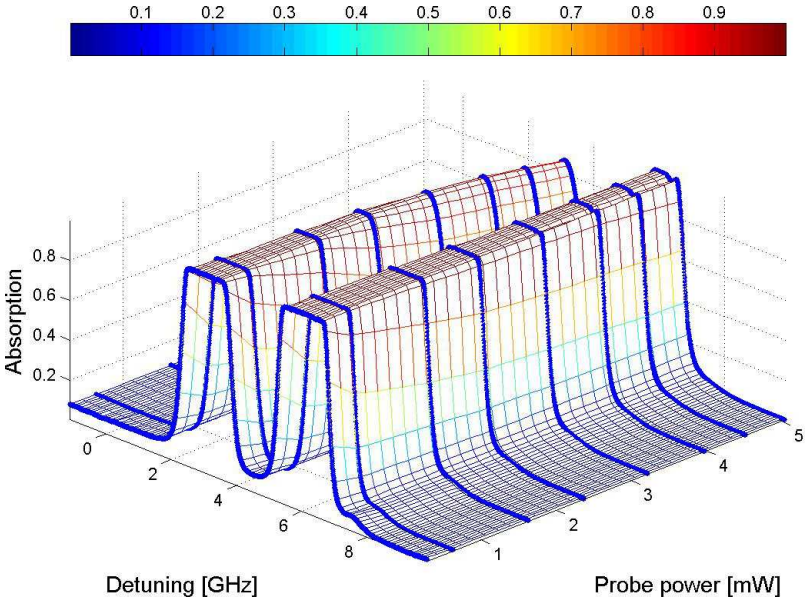

(a) 3D plot of absorption, The data points are shown in blue, with an interpolated grid

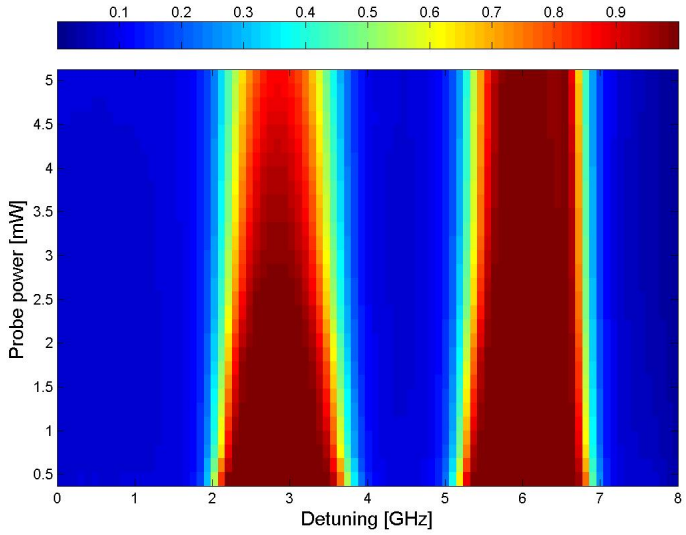

(b) 2D plot of absorption, Interpolated from data in Figure 4.6a

Figure 4.6: Probe power scan: absorption. (The corresponding probe absorption data to Figure 4.5).The absorption signal when the probe frequency was scanned at different probe powers. Cell temperature = 126°C, control 61mW on ^{87}Rb F=1 $\rightarrow$ F'=2 transition, grating spacing = 55 μm.

4.4 Temperature Dependence

With increasing temperature there is an increase in the density of atoms, and also their average velocity and hence Doppler broadening. Overall it was expected that at higher temperatures there will be a increase in the maximum refractive index contrast that can be obtained, δn, and so an increase in the overall efficiency of the grating [28]. This was observed in experiments, see Figure 4.7.

However with increasing temperature there will also be an increase in absorption which will decrease the efficiency. From simulations, in the region of interest, it was expected that increase in the real part of refractive index will be greater than the corresponding increase absorption, and the optimal detuning will shift to the edge of the temperature adjusted absorption. However it is not clear if there will be an optimal temperature, or a limit to the efficiency (below 100%). Although the rate of increase in efficiency was seen to decrease, no maximum was found in these experiments.

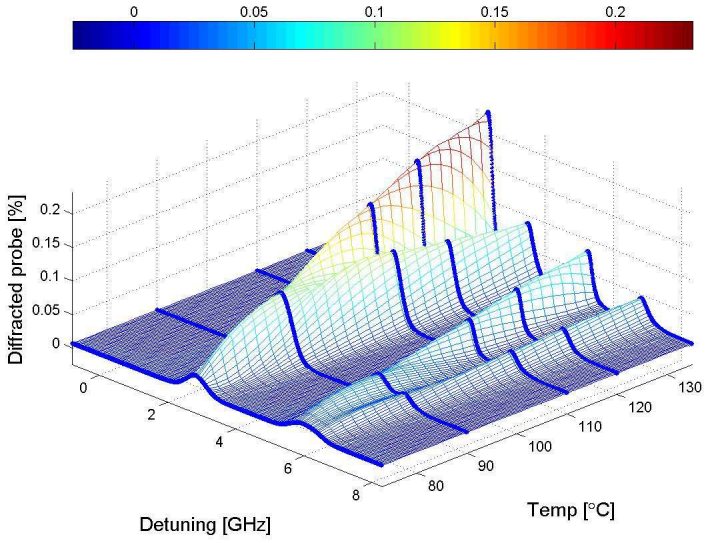

(a) The diffraction efficiency as a function of cell temperature

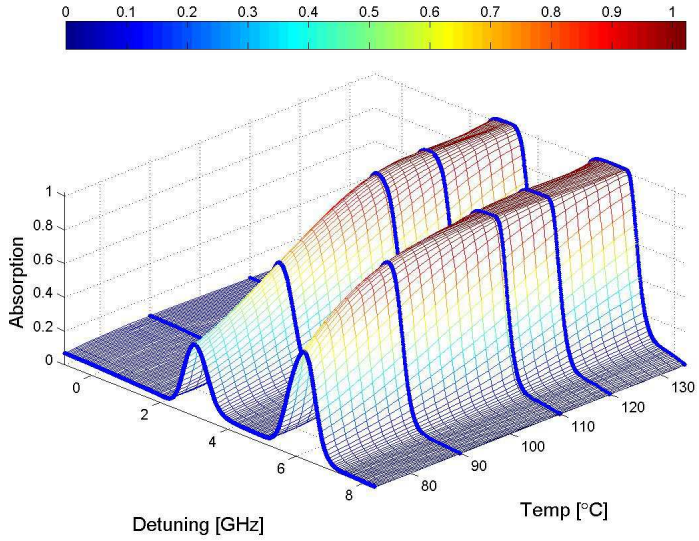

(b) Cell absorption as a function of temperature

Figure 4.7: Change in diffraction response with temperature. The diffraction probe signal when the probe frequency was scanned at different cell temperatures. probe power = 1.1 mW, control power = 50 mW, control on ^{87}Rb F=1 $\rightarrow$ F'=2 transition, grating spacing = 55 μm. The data points are shown in blue, with an interpolated grid

4.5 Control Power Dependence

The results of scanning the total control beam power, Figure 4.8 showed that, as expected, the control power does not affect the overall way that the grating diffracts only the efficiency. By normalizing the response with control power it can be seen that the response is very uniform, consistent with the relationship in Equation 2.25.

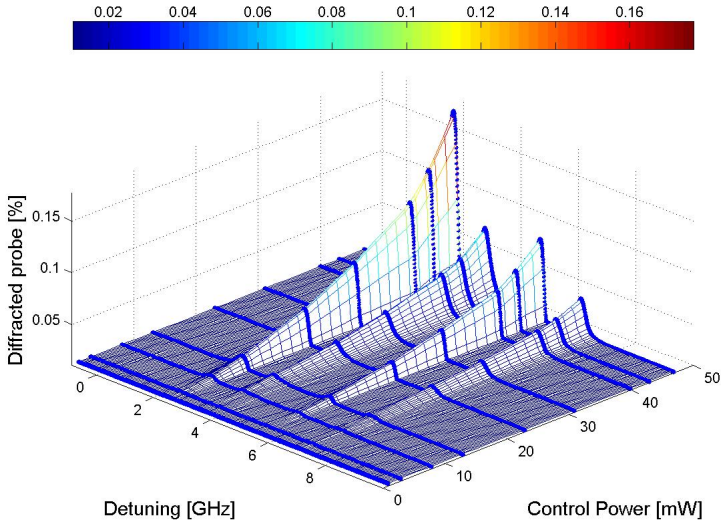

(a) Efficiency of grating

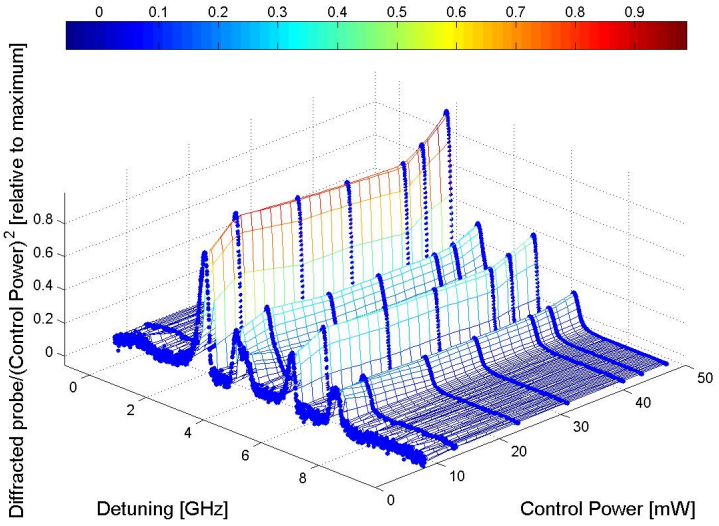

(b) Relative control power adjusted efficiency. $\frac{\text{efficiency}/(control power)^2}{\text{maxefficiency}/(max \text{control} power)^2}$. (Demonstrates consistency with equation 3.8).

Figure 4.8: The diffraction probe signal when the probe frequency was scanned at different control laser powers. cell temperature = 134°C, probe power = 1.4 mW, control control on ^{87}Rb F=1 → F'=2 transition with maximum power = 47 mW, grating spacing = 55 µm. The data points are shown in blue, with an interpolated grid

4.6 Time Domain Response

As discussed in subsection 2.4, it is expected that structures created through the AC Stark shift have potential for fast switching times (of the order of magnitude of the detuning of the control laser). Such response has not yet been observed.

Testing the time domain response of the AC Stark grating proved to be very challenging. The results of the method using an EOM described in section 3.4 are reported. Aside from the fact that an isotopically pure rubidium cell was unavailable for these experiments, additional challenges were presented by drifts in the system. The most problematic drift was the additional phase acquired by the EOM as the temperature fluctuated. Changes to the control laser frequency also presented problems, especially when combined with the natural abundance cell. In order to position the control frequency it was desirable to be on the edge of an absorption line of ^{87}Rb however in this region small fluctuations of the control frequency cause large changes in the diffraction signal. To overcome these challenges, the experiments were carried out in a short time frame (about 20 minutes for each detuning) with efforts made to return to a reference modulation to check and adjust for drifting.

Three signals were compared. One signal had a small detuning ($<$ 1 GHz) with the control laser at the edge of the Doppler broadening, and the grating assumed to be primarily from optical pumping effects of the control laser. The second signal came from a grating where it was not possible to identify the exact detuning of the control laser, only that it was far detuned ($\gtrsim$ 3 GHz) so that none of the characteristic resonance phenomena occurred and no change in the diffraction signal occurred even with significant changes to the control laser current. In the third grating the control laser was positioned on the edge of the Doppler profile of the ^{87}Rb $F = 2 \rightarrow F' = 2$ transition, and the signal from the ^{85}Rb F=3$\rightarrow$F'=2 was measured (about 1.5 GHz detuning).

The results are summarized in Figure 4.9. The main feature was that for the small detuned grating most of the modulations died out by 50 MHz consistent with an optical pumping grating. A small residue signal continued up to 800 MHz (not shown), that could be explained by the small amount of Stark shifting within the optical pumping grating. However for the gratings produced by larger detunings all the modulations completely died out by around 50 MHz. It is suggested that the bandwidth of the diffraction is limited by the width of the response. As faster modulations have a larger range of frequencies, if the bandwidth of the response is too small the range of frequencies will be unable to undergo diffraction (they will either be absorbed or will not experience a sufficient index contrast). Thus the optical pumping grating had a larger bandwidth (O(GHz)) and this allowed for the faster Stark modulations whereas the further detuned gratings had a very low diffraction efficiency and a very narrow bandwidth and so did not allow for fast modulations. The difference in fits of the responses, Figure 4.9, may be related to the different underlying mechanisms in the gratings, as the larger detuned gratings may be responding as a result of the bandwidth limitation of the diffraction, whereas the small detuned grating is limited by the optical pumping response time.

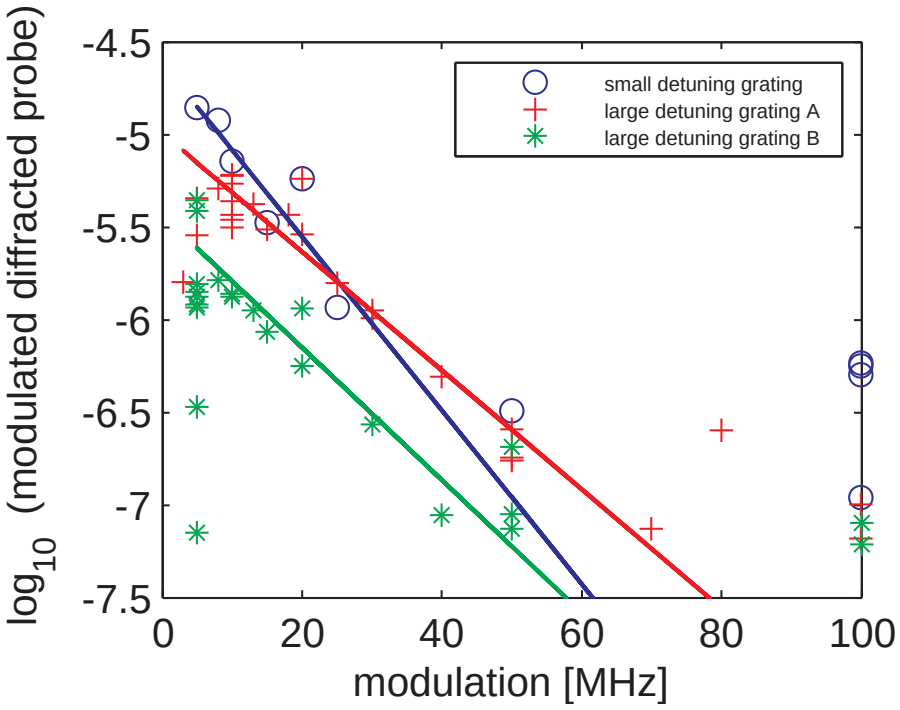

Figure 4.9: Time Domain Response

5 Conclusions & Future Work

Summary

An electromagnetically induced thick Bragg grating has been produced using the AC Stark Effect. This has been achieved by finding the the correct parameters of atomic density, and control laser intensity and arrangement. Diffraction from this grating has been observed for a probe laser close to the ^{85}Rb D_1 lines when the rubidium was heated to around 100 °C, and the control laser was far detuned from these lines ($>$ 1 GHz). The behavior of this grating was consistent with the AC Stark effect. This was demonstrated through the consistency with theory, where the greatest signal occurred on the edge of the transmission profile, and the consistency with simulation. The efficiency also behaved in accordance with expected change in control detuning and intensity.

These structures were expected to have fast ($>$ 1 ns) response times, however evidence of this has not yet been found. Attempts have been made to explain the subtleties of the effect by considering the optical pumping of the probe, counter-propagating probe and control, hole burning and absorption grating.

Experimental Improvements

The most obvious improvements would be to improve the efficiency and stability of the device. This would enable more conclusive time domain experiments. With the current equipment, it would seem that greater efficiency could be achieved by improved fitting of the probe dimensions to the dimensions of the grating, so that the probe passes through a region of higher refractive index contrast.

With additional equipment, a more powerful control laser would produce a greater AC Stark shift and higher efficiency. It should also be possible to increase the efficiency of the grating by heating the cell to a higher temperature (this would require a special cell as experience has shown the limits of a standard cell to be about 140°C). Simulations also indicate that an increased cell length would improve the efficiency.

The stability of the system could be improved by using an amplitude EOM, with two electro-optic crystals to compensate for the temperature drifting. Additionally a more stable control laser would aid in the measurement process. In the current laser, home built ECDL, the main drift seems, due to the time scale of the drifts, to come from temperature fluctuations and improving the temperature stability may be a way to improve the frequency stability.

Future Directions and Limitations

It would seem that the main utility of this device would lie in its control speed. The fundamental limits to the time response of such a structure could come from two sources, inherently from the

AC Stark effect and indirectly from the geometry of the constructed structure.

Theoretically the switching time should be limited by the AC Stark effect which scales as $1/\Delta$. A faster switching time can be achieved by using a larger detuning. This will involve using a greater intensity to achieve a significant Stark shift. It should be possible to avoid the effects of additional optical pumping caused by the increased intensity, as optical pumping scales as (I/Δ^2) so increasing the intensity and hence optical pumping can be compensated for by a larger detuning. It also appears that there will be a limit to the time response from the width of the response of the refractive index contrast.

The created structure will also have a limit from its dimensions, for instance it takes light about 250 ps to traverse 7.5 cm. The current design will also be limited by the condition of the diffracting Bragg angle. At large switching speeds the different frequency components will start to have significantly different Bragg angles thus limiting the switching time.

Theoretically it should be possible to build any structure according to the light intensity. This will require 'structuring' the light in the required pattern, which will have the additional challenge of maintaining a high intensity.

Such fast control of light may find uses with control of quantum pulses or maybe even in the transfer of classical information. However practical uses will require greater efficiencies.

6 Appendices

6.1 Calculating the Susceptibility

At different stages of the work various 'versions' of equation 2.5 were used to calculate the refractive index.

For initial calculations to estimate the magnitude of the AC Stark effect equation 2.5 with and without the estimated AC Stark shift was used. The atomic density was calculated using appropriate equation in Reference [27]. When simulating the experimental results the diffracted signal in order to understand the relative heights of diffraction peaks other factors were included. This involved giving a weight for the relative line strengths and populations for each transition weights for each of the transitions in ^{85}Rb D1 transitions $\mathrm{F_g} = 2, 3 \rightarrow \mathrm{F_e} = 2, 3$ giving $\mathrm{c_{jk}}$ and $\mathrm{g_j}$ [27] and an appropriate term to allow for hole burning was also added [21]. For the Doppler broadening, the temperature measured during the experiment was used while for the atomic density a phenomenologically lower temperature was used for calculating the atomic density, subsection 4.3, which was believed to be caused by optical pumping from the probe. Additionally allowance was made in calculating the Stark shift for the counter propagating nature of the control and probe beams. This gives a Stark susceptibility of

$$\begin{aligned}\chi_s(\omega) = N(\mathrm{T}) \sum_{j=2,3} \sum_{k=2,3} g_j c_{jk} D \int \frac{1}{(1+2\mathrm{i}\gamma(\omega-((\omega_{jk}+\Delta\omega_{jk}))} \\ \times exp\left(-4ln2\left(\frac{\omega'-\omega_{jk}}{\Delta\omega_d}\right)^2\right) \times \frac{1}{1+\mathcal{L}\mathcal{I}} d\omega'\end{aligned} \tag{6.1}$$

where the last term in the integral involving the Lorentzian, $\mathcal{L}$, and the dimensionless intensity, $\mathcal{I}$, simulate the hole burning and are taken from reference [21]

$$\mathcal{L} = \frac{1}{1+\Delta\mathrm{T}_2'} \tag{6.2}$$

$$\mathcal{I} = 4\Omega_\mathrm{p}^2 \mathrm{T}_1 \mathrm{T}_{2'} \tag{6.3}$$

This equation was evaluated in MATLAB using the 'trapz' function (which was chosen to help with normalization)

The basic MATLAB code for a Stark shifted transition was

```
widthGHZ =12;                                                    % range of calculation in GHz
width = widthGHZ*1e9;                                                                    % Hz
detuning = -width/2:  1E7:  +width /2-1E7;
om = -width/2:  1E6:  +width /2-1E6;                    % set up vector for dummy variable
wa= 2*pi*om;  %
z1 = length(detuning);                                                % loop for calculation
for r=1:z1 ;
w = 2*pi*detuning(r) ;                                    % conversion to angular frequency
L1 = 1./(1+((w-wa)*T2t/2/pi).^2);                  % saturation effects based on reference [21]
y1=exp(-4*log(2)*((wa-shift1)/Dwd).^2)
./(1+2*1i*(w-(wa-2*pi*RABIHZ^2./2./(detuningpump-wa/2/pi+2*shift1/2/pi)))/Dwa)
.*(1./(1+L1*II));              % an appropriate term for each of the 85Rb transitions was used,
                                                    RABIHZ was the Rabi frequency of the control laser,
                                  the term for the control laser detuning considers the detuning of the laser
                                                    from the 85Rb F=2→F'=3 transition
                                                    the relative shift of each 85Rb transition,
                                  and the counter propagating nature of the control and probe
y= g2*(S23*y1+S22*y2) +g3*(S33*y3+S32*y4);      %Four similar terms were added      with
appropriate weighting,
XS(r) = CONST*trapz(wa,y);          %The Stark susceptibility is the solution of the integration
                                  multiplied by a constant including the appropriate prefactors
                                                    including the temperature appropriate atomic density
end
```

It should be noted that this code gave a sign error for the imaginary part of the susceptibility that was corrected manually.

6.2 Simulating the light propagation

The propagation of light through the grating was simulated by MATLAB script based upon the spatial Fourier component and the propagation transfer function [31]. Using this transfer function a 2D array representing a Gaussian beam was propagated through space. In the grating region an appropriate phase was added to the profile.

The MATLAB code for the transfer function was % fx, fy spatial fourier components

```
function phi = h2(fx,fy,d2,lam)                          % fx, fy - spatial fourier components
                                                                        % d2 - propagation distance
                                                                        % lam - wavelength of light
dg=1/lam^2 - fx .^2 - fy .^ 2;
phi = exp(i * 2 * pi * d2 .* sqrt(dg));
```

An additional phase, in real space was added in the grating region, with the changes proportional to the grating intensity, I

```
phaseshift=exp(-i*(2*pi/lambda)*dn*I*dzint/2).*
exp((alpha)*dzint/2).*exp(dalpha*I*dzint/2);
```

The different diffraction orders were comparing orders were compared by summing the absolute values of the square of the pixels in that order.

6.3 Converting a phase EOM to amplitude EOM

The experiment for the time modulation a phase EOM had to be converted to an amplitude EOM. It is well known [2] that placing an electro-optic crystal between crossed polarizer allows for amplitude modulation of the light. Maximal modulation will occur when the crossed polarizers are at 45° to the electrically induced principal axes, and a fixed $\lambda/4$ retardation plate was aligned with these axes. However it was not clear how to align the polarization optics if the crossed polarizers were not at 45° to the axis of the EOM, which would be the case in the experimental set-up.

In order to answer this question the following Jones matrix equation was solved

$$\mathrm{O} = \mathrm{P} \cdot \mathrm{R}(\theta_3) \cdot \mathrm{R}(-\theta_2) \cdot \mathrm{WP}(\frac{\lambda}{4}) \cdot \mathrm{R}(\theta_2) \cdot \mathrm{EOM(V)} \cdot \mathrm{R}(-\theta_1) \cdot \mathrm{WP}(\frac{\lambda}{2}) \cdot \mathrm{R}(\theta_1) \cdot \mathrm{I} \tag{6.4}$$

where I and O are the input and output Jones vectors,

polarizer $\mathrm{P} = \begin{pmatrix} 1 & 0 \\ 0 & 0 \end{pmatrix}$,

rotation matrix $\mathrm{R}(\theta) = \begin{pmatrix} \cos\theta & \sin\theta \\ -\sin\theta & \cos\theta \end{pmatrix}$,

phase modulation, waveplate $\mathrm{WP}(\frac{\lambda}{\mathrm{N}}) = \begin{pmatrix} \exp\left(-i\frac{\pi}{N}\right) & 0 \\ 0 & \exp\left(-i\frac{\pi}{N}\right) \end{pmatrix}$,

$$\texttt{EOM} = \begin{pmatrix} \exp\left(-i\frac{\mathrm{V}}{\mathrm{V}_\pi}\frac{\pi}{2}\right) & 0 \\ 0 & \exp\left(-i\frac{\mathrm{V}}{\mathrm{V}_\pi}\frac{\pi}{2}\right) \end{pmatrix}$$

Showed that 2 rotatable wave plates were sufficient to achieve maximal modulation.

However maximum modulation does not occur at maximum intensity (and hence diffracted signal). This calculation also showed where an optimum balance between signal and modulation could be achieved.

Implementation of this scheme proved difficult because of temperature drifts, that caused expansion of the crystal in the modulator and hence gave an arbitrary phase shift to the light. Attempts were made to stabilize the EOM with PID control, but they were unable to sufficiently stabilize the system. However it was known that the phase drift could be compensated for by the phase plates.

6.4 PID Control

Work was done to control the stability of different systems in the experimental set-up. Primarily the temperature of the ECDL and the EOM. This involved working with PID control. The basic idea is that a control variable, c(t) will be fed back into the system. The size of this control will depend

upon an error signal, e(t), equal to the difference between a measured signal from the system and a reference (the required output). The exact size of this control will be related to the size of the error - proportional (P), its integral (I), and differential (D)

$$c(t) = K_p e(t) + K_i \int^t e(\tau)\mathrm{d}\tau + K_d \frac{\mathrm{d}}{\mathrm{dt}} e(t) \tag{6.5}$$

Depending upon the system and the values of the constants, oscillations and other unwanted phenomena can occur. It is believed that a poor integral control of the temperature allowed for drifts of the control laser frequency over time. Without an integral component there will be a steady-state offset between the actual value and the required value. With a changing external environment (temperature) this difference will drift causing changes to the lasing frequency and mode hops. The subject of PID control is huge and fascinating an excellent book was found to be "Feedback Systems: An Introduction for Scientists and Engineers" [32].

6.5 Publication

Together with with results of an AC Stark photonic band gap, the results of collaborators in Prof John Howells group in University of Rochester, the main results of this work have been accepted for publication in Physics Review A. The article is available on the archive: http://arxiv.org/abs/1301.6380

References

[1] M. Born, E. Wolf, and A.B. Bhatia. *Principles of Optics: Electromagnetic Theory of Propagation, Interference and Diffraction of Light*. Cambridge University Press, 1999.

[2] A. Yariv and P. Yeh. *Photonics: Optical Electronics in Modern Communications*. The Oxford Series in Electrical and Computer Engineering. Oxford University Press, 2007.

[3] J. Frejlich. *Photorefractive Materials: Fundamental Concepts, Holographic Recording and Materials Characterization*. Wiley, 2007.

[4] A. G. Truscott, M. E. J. Friese, N. R. Heckenberg, and H. Rubinsztein-Dunlop. Optically written waveguide in an atomic vapor. *Phys. Rev. Lett.*, 82:1438–1441, Feb 1999.

[5] N. Korneev and O. Benavides. Mechanisms of holographic recording in rubidium vapor close to resonance. *J. Opt. Soc. Am. B*, 25(11):1899–1906, Nov 2008.

[6] D. M. Bloom, P. F. Liao, and N. P. Economou. Observation of amplified reflection by degenerate four-wave mixing in atomic sodium vapor. *Opt. Lett.*, 2(3):58–60, Mar 1978.

[7] N. Korneev and Jose Soto. The nonlinear faraday rotation-based dynamic holography in rubidium vapor. *Optics Communications*, 245:437 – 442, 2005.

[8] P. R. Hemmer, D. P. Katz, J. Donoghue, M. Cronin-Golomb, M. S. Shahriar, and P. Kumar. Efficient low-intensity optical phase conjugation based on coherent population trapping in sodium. *Opt. Lett.*, 20(9):982–984, May 1995.

[9] Hong Yuan Ling, Yong-Qing Li, and Min Xiao. Electromagnetically induced grating: Homogeneously broadened medium. *Phys. Rev. A*, 57:1338–1344, Feb 1998.

[10] Masaharu Mitsunaga and Nobuyuki Imoto. Observation of an electromagnetically induced grating in cold sodium atoms. *Phys. Rev. A*, 59:4773–4776, Jun 1999.

[11] Andy W. Brown and Min Xiao. All-optical switching and routing based on an electromagnetically induced absorption grating. *Opt. Lett.*, 30(7):699–701, Apr 2005.

[12] Praveen K. Vudyasetu, David J. Starling, and John C. Howell. All optical waveguiding in a coherent atomic rubidium vapor. *Phys. Rev. Lett.*, 102:123602, Mar 2009.

[13] M. Artoni and G. C. La Rocca. Optically tunable photonic stop bands in homogeneous absorbing media. *Phys. Rev. Lett.*, 96:073905, Feb 2006.

[14] Aharon J. Agranat. Electroholographic wavelength selective switches in wdm networks. available at http://aph.huji.ac.il/people/agranat/lab/Concepts.html, 2001.

[15] Dmitry Budker, Donald J. Orlando, and Valeriy Yashchuk. Nonlinear laser spectroscopy and magneto-optics. *Am. J. Phys.*, 67:584, 1999.

[16] David J. Starling, Steven M. Bloch, Praveen K. Vudyasetu, Joseph S. Choi, Bethany Little, and John C. Howell. Double lorentzian atomic prism. *Phys. Rev. A*, 86:023826, Aug 2012.

[17] A.E. Siegman. *Lasers*. University Science Books, 1986.

[18] Robert W. Boyd and Murray Sargent. Population pulsations and the dynamic stark effect. *J. Opt. Soc. Am. B*, 5:99–111, 1988.

[19] R.W. Boyd. *Nonlinear Optics*. Academic Press. Elsevier Science, 2008.

[20] J.J. Sakurai. *Modern Quantum Mechanics*. Pearson Education, 2006.

[21] L. Allen and J.H. Eberly. *Optical Resonance and Two-Level Atoms*. Dover Books on Physics. Dover, 1975.

[22] Benjamin J. Sussman. Five ways to the nonresonant dynamic stark effect. *Am. J. Phys*, 79:477, 2011.

[23] R. Loudon. *The quantum theory of light*. Oxford science publications. Clarendon Press, 1983.

[24] C. Cohen-Tannoudji, J. Dupont-Roc, and G. Grynberg. *Atom-Photon Interactions*. Wiley Science Paperback Series. Wiley, 1998.

[25] M. A. Jones. Atom light interactions. available at http://massey.dur.ac.uk/mpaj/notes_main.pdf.

[26] William Happer. Optical pumping. *Rev. Mod. Phys.*, 44:169–249, Apr 1972.

[27] Daniel A. Steck. Rubidium 85 d line data. available online at http://steck.us/alkalidata, September 2012.

[28] Kogelnik. Coupled wave theory for thick hologram gratings. *The Bell System Technical Journal*, 48:2909, 1969.

[29] Daryl W. Preston. Dopplerfree saturated absorption: Laser spectroscopy. *Am. J. Phys*, 64:1432, 1996.

[30] K. B. MacAdam, A. Steinbach, and C. Wieman. A narrowband tunable diode laser system with grating feedback, and a saturated absorption spectrometer for cs and rb. *Am. J. Phys*, 60:1098, 1992.

[31] J.W. Goodman. *Introduction To Fourier Optics*. McGraw-Hill physical and quantum electronics series. Roberts & Co., 2005.

[32] K. J. Åström and R. M. Murray. *Feedback Systems: An Introduction for Scientists and Engineers*. Princeton University Press, 2008. Available online at http://press.princeton.edu/titles/8701.html.